

Characterization of proton-induced damage in thick, p-channel skipper-CCDs

Brenda A. Cervantes-Vergara^{*a}, Santiago E. Perez^{b,c}, Claudio Chavez^a, Fernando Chierchie^d, Brandon Roach^e, Juan Estrada^{a,f}, and Alex Drlica-Wagner^{a,e,f}

^a*Fermi National Accelerator Laboratory, Batavia, IL, USA*

^b*Facultad de Ciencias Exactas y Naturales, Departamento de Física, Universidad de Buenos Aires, Buenos Aires, Argentina*

^c*Instituto de Física de Buenos Aires (IFIBA), CONICET - Universidad de Buenos Aires, Buenos Aires, Argentina*

^d*Instituto de Inv. en Ing. Eléctrica “Alfredo C. Desages” (IEEE), CONICET, Bahía Blanca, Argentina*

^e*Kavli Institute for Cosmological Physics, University of Chicago, Chicago, IL, USA*

^f*Department of Astronomy and Astrophysics, University of Chicago, Chicago, IL, USA*

Abstract

In this work, we characterize the radiation-induced damage in two thick, p-channel skipper-CCDs irradiated unbiased and at room temperature with 217-MeV protons. We evaluate the overall performance of the sensors and demonstrate their single-electron/single-photon sensitivity after receiving a fluence on the order of 10^{10} protons/cm². Using the pocket-pumping technique, we quantify and characterize the proton-induced defects from displacement damage. We report an overall trap density of 0.134 traps/pixel for a displacement damage dose of 2.3×10^7 MeV/g. Three main proton-induced trap species were identified, V_2 , C_iO_i and V_nO_m , and their characteristic trap energies and cross sections were extracted. We found that while divacancies are the most common proton-induced defects, C_iO_i defects have a greater impact on charge integrity at typical operating temperatures because their emission-time constants are comparable or larger than typical readout times. To estimate ionization damage, we measure the characteristic output transistor curves. We found no threshold voltage shifts after irradiation. Our results highlight the potential of skipper-CCDs for applications requiring high-radiation tolerance and can be used to find the operating conditions in which effects of radiation-induced damage are mitigated.

1 Introduction

Charge-Coupled Devices (CCDs), pixelated ionization sensors, are a well-established technology widely used in various scientific applications due to their attractive features, including high quantum efficiency, low dark counts, and low readout noise. Skipper-CCDs combine these features with the added advantage of single-electron/single-photon sensitivity, enabled by their ability to perform multiple non-destructive measurements of the charge in each pixel. This technology has demonstrated excellent performance in applications requiring sensitivity to faint signals, such as direct dark matter detection [1, 2, 3] and astronomical spectroscopy [4]. To extend its use to scientific applications where detectors are expected to operate in high-radiation environments, such as space missions or accelerator-based experiments, it is essential to demonstrate and quantify its radiation tolerance.

Studies on total dose radiation damage in silicon detectors [5, 6], and particularly in CCDs [7, 8, 9, 10], are extensive, and generally classify it into two types: ionization damage and displacement damage. On one hand, ionization damage primarily degrades the insulator layer by creating interface defects and trapped

*bcervant@fnal.gov

charge within the layer. Interface defects can lead to higher surface dark counts, and trapped charge can lead to voltage shifts causing charge-transfer inefficiency (CTI) between pixels or changes in the operating point of the CCD transistors. On the other hand, displacement damage produces vacancy-interstitial pairs which later form more stable defects within the bulk, such as divacancies and vacancy-impurity complexes, that create intermediate energy levels acting as charge traps. This damage can induce CTI and higher dark counts from hot pixels, the latter primarily promoted by defects with an energy level close to midgap.

The susceptibility of CCDs to ionization damage varies significantly depending on their design and the irradiation conditions. In most cases, the effects of this damage can be mitigated, making displacement damage the primary limiting factor for CCD applications in high-radiation environments [9]. Regarding displacement damage, studies indicate that p-channel CCDs are radiation harder than n-channel CCDs due to the characteristics of the induced defects [11, 12, 13, 14]. The dominant radiation-generated trap in n-channel CCDs is the phosphorous-vacancy (PV) electron trap [15], while in p-channel CCDs, it is the divacancy (V_2) hole trap [11]. P-channel CCDs are considered radiation harder because: 1) the formation of V_2 traps in p-channel CCDs is predicted to be less favorable compared to the formation of PV traps in n-channel CCDs [14], and 2) the PV trap energy ($\sim 0.42 - 0.46$ eV below the conduction band) is closer to midgap than the V_2 trap energy ($\sim 0.21 - 0.23$ eV above the valence band), leading to higher dark counts in n-channel CCDs.

2 Proton irradiation of skipper-CCDs

The sensors tested in this work are thick, p-channel skipper-CCDs, fabricated from high-resistivity n-type silicon, designed at the Lawrence Berkeley National Laboratory (LBNL) in collaboration with the Fermi National Accelerator Laboratory (FNAL) during the R&D phases of the SENSEI and Oscura [16] dark matter experiments, and fabricated in two different foundries. Each sensor features an array of three-phase $15 \times 15 \mu\text{m}^2$ pixels, and four floating-gate readout amplifiers, one in each corner. The sensors were irradiated unbiased and at room temperature at the Northwestern Medicine Proton Center in Warrenville, Illinois, in August 2023, using a 217-MeV proton cyclotron; for details, see Ref. [17]. To ensure a baseline for comparison, at least a region within the sensor active area and a couple of readout amplifiers of each sensor were kept outside the proton beam line during irradiation as shown in Fig. 1.

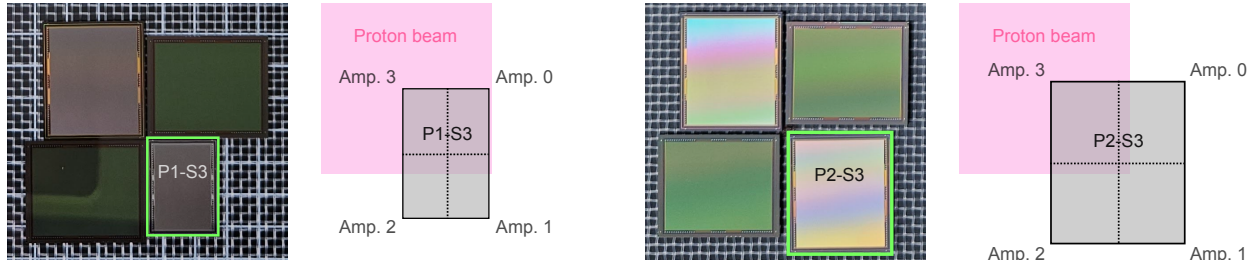


Figure 1: Pictures of the irradiated skipper-CCDs (the sensors tested in this work are highlighted in green) and drawings showing the approximate area irradiated by the proton beam (pink) in each sensor (gray).

Proton fluences were chosen to reach displacement damage doses (DDD) higher than the estimated for the SNAP satellite orbiting at the second Earth-Sun Lagrange point (L2) for six years, i.e. 6.6×10^6 MeV/g (Si) [18]. We compute the expected DDD for each fluence assuming a non-ionizing energy loss (NIEL) factor of 1.9×10^{-3} MeV cm^2/g for 217-MeV protons in silicon [19]. The expected total ionizing dose (TID) for each fluence was computed assuming an electronic stopping power of 3.456 (3.605) MeV cm^2/g for 217-MeV protons in silicon (silicon dioxide) [19]. Table 1 summarizes the main characteristics of the sensors tested in this work, the proton fluences they were irradiated with, and their expected damage doses.

Sensor ID	Pixel array size	Thickness	Fluence [p/cm ²]	DDD [10 ⁸ MeV/g]	TID [10 ¹¹ MeV/g]
P1-S3	1022 × 682	675 μm	1.2 × 10 ¹⁰	0.23 (Si)	0.41 (Si), 0.43 (SiO ₂)
P2-S3	1278 × 1058	725 μm	8.4 × 10 ¹⁰	1.60 (Si)	2.90 (Si), 3.03 (SiO ₂)

Table 1: Geometrical characteristics of the tested sensors, the proton fluences they were irradiated with, and their expected damage doses.

3 Characterization of proton-induced damage

The irradiated sensors were packaged and tested at FNAL. For packaging, the sensor and a Kapton flex cable are glued to a silicon substrate, and the sensor is wire-bonded to the cable. The assembly, consisting of the sensor, flex cable, and substrate, is enclosed within a two-piece copper tray, forming a packaged sensor. For testing, each packaged sensor is mechanically attached to the cold tip of a cryocooler located inside a vacuum chamber. The sensor’s flex cable connects to a feedthrough connector on the vacuum side of the chamber, which in turn connects to a Low Threshold Acquisition (LTA) electronics board [20] on the air side. This board is used for sensor control and readout. During testing, the vacuum chamber is evacuated to a pressure of $\sim 1 \times 10^{-5}$ mbar, and the sensor is cooled to typical operating temperatures, i.e. ~ 150 K. We read out the sensors using all four amplifiers, one per CCD quadrant.

3.1 Overall performance

Dark exposures of the sensors were taken using the typical operating voltages. To evaluate the performance of each amplifier, we tested their ability to perform multiple non-destructive measurements by taking a set of images with different number of samples per pixel N_{smp} . The readout noise for each image was computed from the offset-subtracted pixel distribution as the standard deviation of a Gaussian fit centered at zero. We plot this noise as a function of N_{smp} and fit the data with the function $\sigma_0(N_{\text{smp}})^{-\alpha}$, where σ_0 and α are free parameters representing the single-sample noise and the power-law exponent. The readout noise data and corresponding fits for each amplifier in the tested sensors are shown in Fig. 2.

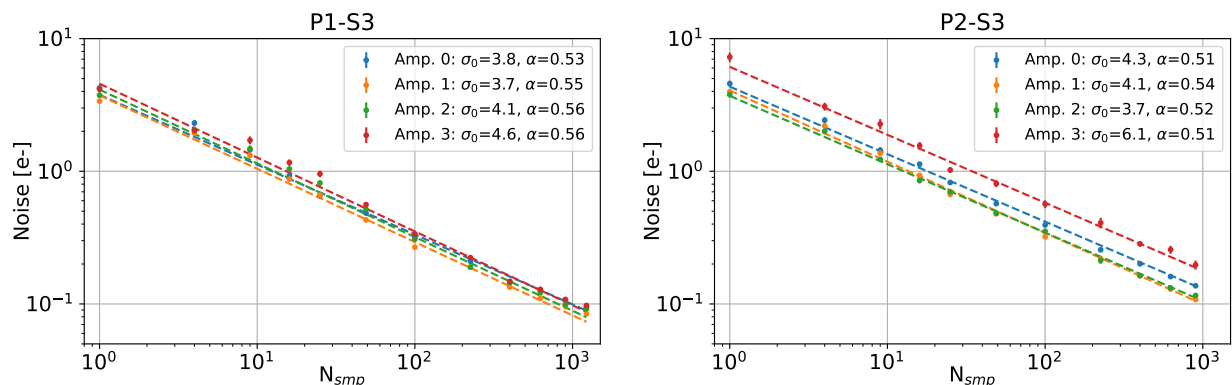


Figure 2: Readout noise as a function of N_{smp} for each amplifier in the irradiated sensors and their corresponding best fit with the function $\sigma_0(N_{\text{smp}})^{-\alpha}$.

The readout noise for all amplifiers in both sensors decreased with increasing N_{smp} , reaching sub-electron noise levels for $N_{\text{smp}} > 11$ (35) samples/pixel in the best (worst) case. In both sensors, amplifier 3 exhibited the highest single-sample noise, comparing the fits. These amplifiers were also located closest to the center of the proton beam area during irradiation. For all amplifiers, $0.51 \leq \alpha \leq 0.56$, which is expected for low-frequency noise with components $1/f^n$ for $1 \leq n < 2$ [21].

Evident features of radiation damage were clearly observed in the sensors’ active area within the proton beam area when sub-electron resolution was achieved. In standard CCDs, charge trapping and emission of single-electron traps caused by displacement damage manifest as increased dark counts or CTI. In skipper-CCDs, however, the combination of sub-electron energy resolution and the inherent spatial resolution of pixelated sensors reveals individual non-empty pixels with few-electron depositions, enabling precise spatial identification of effects from radiation-induced defects. These effects are also visible in the pixel charge distributions, where discrete peaks at few electrons are more pronounced for the quadrants that were within the beam area during irradiation, i.e. those read through amplifiers 0 and 3 for P1-S3 and through amplifier 0 for P2-S3, as shown in Fig. 4.

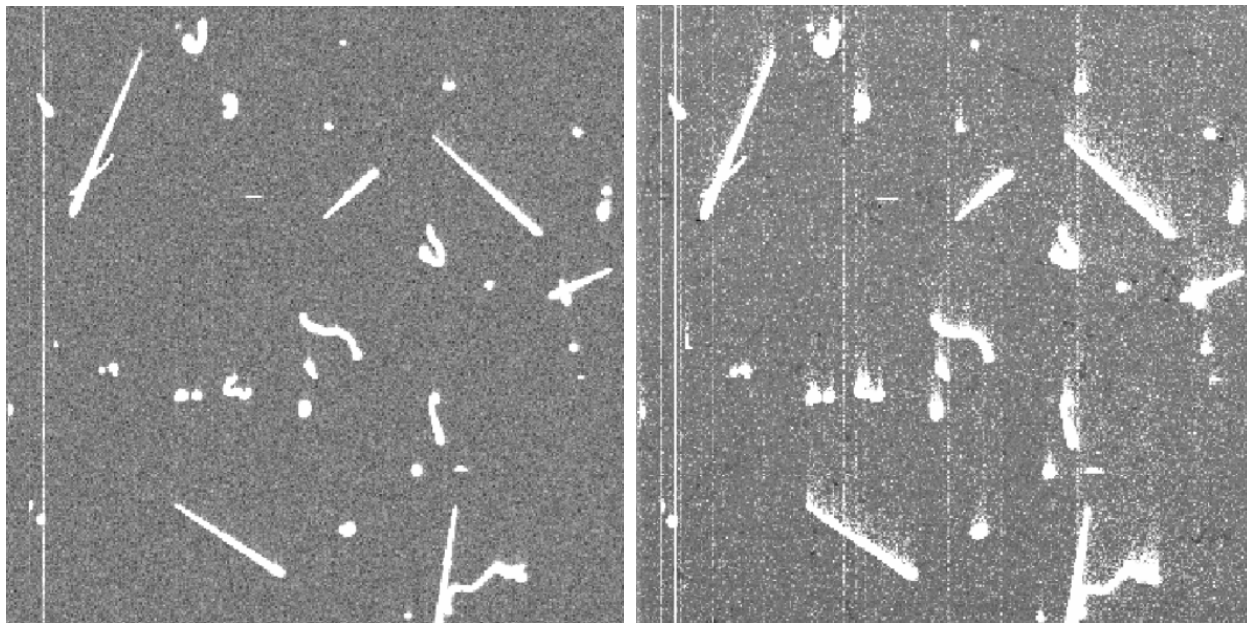


Figure 3: Region of a dark exposure image from sensor P1-S3 ($340 \text{ pix} \times 340 \text{ pix}$) acquired with $N_{\text{smp}} = 225$ samples/pixel through amplifier 0. In the left image, each pixel value corresponds to a single charge measurement, while in the right image, each pixel value is the average of all 225 measurements. Particle tracks from cosmic radiation interactions are clearly seen in both images, but few-electron depositions from proton-induced damage are only visible in the right image due to the single-electron resolution.

3.2 Displacement damage

Pocket pumping measurements

Pocket pumping [21, 22, 23, 24] is a powerful technique for spatially localizing and characterizing charge traps in CCDs. It involves repeatedly moving charge between pixel phases, allowing multiple cycles of charge capture and emission that produce identifiable “dipole” signals. We use this technique to localize and characterize proton-induced traps from displacement damage, following a procedure analogous to that described in Ref. [25]. We illuminate the sensor to be tested with a violet LED, providing a relatively uniform charge distribution between $1500\text{--}2000 e^-/\text{pixel}$, and we perform an optimized pocket pumping sequence to probe traps under pixel phases 1 and 3. Sensors were read using all four amplifiers with $N_{\text{smp}} = 10$ samples/pixel. We collected images with $N_{\text{pumps}} = 2000$ pumping cycles, varying the pumping time t_{ph} between $0.6 \mu\text{s}$ to 1 s. We took data at different temperatures, from 140K to 200K.

After subtracting the median pixel value of each row and column in the image, we apply a dipole detection algorithm previously used in Ref. [25]. This algorithm searches for two consecutive pixels in each column

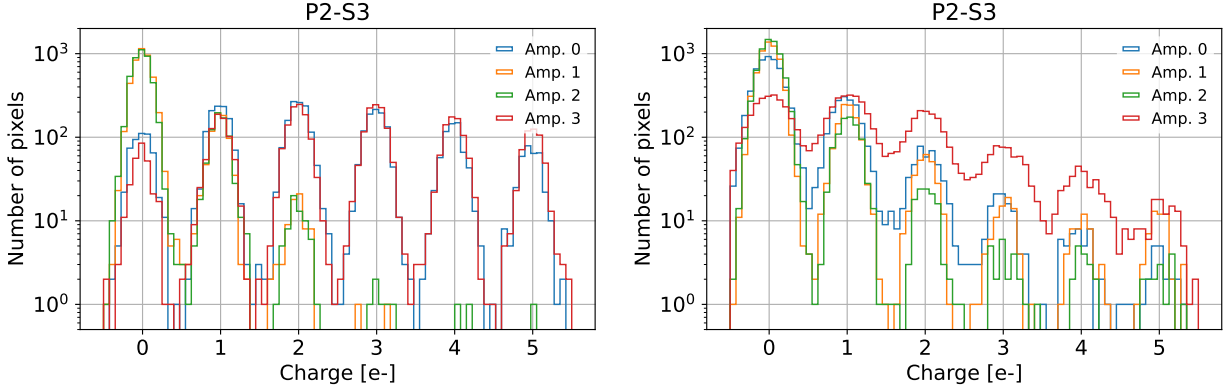


Figure 4: Pixel charge distributions from dark exposure images, acquired with $N_{\text{smpl}} = 625$ samples/pixel, corresponding to data read through each amplifier in sensor P1-S3 (left) and sensor P2-S3 (right). Larger pixel values are evident from regions that were within the beam area during irradiation, i.e. those read through amplifiers 0 and 3 for P1-S3 and through amplifier 0 for P2-S3.

that meet the following criteria: their values have opposite signs and are symmetrical with respect to zero, and their amplitude \mathcal{A} , calculated as the absolute value of the difference between their pixel values, is at least five times the median amplitude of any two consecutive pixels in the same column.

Using sets of images from the same sensor acquired at a fixed temperature, we compute the dipole intensity $I_{\text{dip}} = \mathcal{A}/2$ as a function of t_{ph} for each detected dipole. We fit this curve with the following equation,

$$I_{\text{dip}} = \mathcal{C} \left(e^{-\frac{t_{ph}}{\tau_e}} - e^{-8\frac{t_{ph}}{\tau_e}} \right), \quad (1)$$

which is valid for the optimized pocket pumping sequence that we performed [24], with \mathcal{C} a constant given by the product of N_{pumps} , the trap depth and the probability of charge capture. From the fit, we extract the trap emission-time constant τ_e associated with the dipole. We select fits with a coefficient of determination greater than 0.7 and a relative error on τ_e below 50%. The histograms of the emission-time constants for the detected dipoles that passed the selection cuts, i.e. the “selected dipoles”, in a $240 \text{ pix} \times 240 \text{ pix}$ region read through amplifiers 1 and 3 in each sensor and at different temperatures are shown in Fig. 5.

In all the τ_e distributions in Fig. 5, several peaks are observed. The peaks common to both sensors are associated with proton-induced traps, which exhibit emission-time constants ranging from a few microseconds to a few seconds at the tested temperatures. Additional peaks appearing in sensor P2-S3 have been associated in previous work with defects from fabrication [25], with emission-time constants from milliseconds to seconds.

The number of selected dipoles associated with proton radiation damage is higher in the region next to amplifier 3 compared to the region next to amplifier 1 in both sensors. This is expected, as the region next to amplifier 3 was within the proton beam area during irradiation. Although sensor P2-S3 received a higher fluence than sensor P1-S3 during irradiation, resulting in more proton-induced traps, the number of selected dipoles associated with these traps in the histograms in Fig. 5 is lower for sensor P2-S3 than for sensor P1-S3. This discrepancy arises from differences in the detection and selection efficiencies of dipoles, which are lower for sensor P2-S3 due to the higher trap density in pocket-pumped images caused by the combined presence of fabrication and proton-induced traps. The difference in efficiencies also explains why the number of selected dipoles corresponding to fabrication traps in sensor P2-S3 is higher for the region next to amplifier 1 than for the region next to amplifier 3, where the significantly higher trap density leads to lower efficiencies.

As the detection efficiency is higher for sensor P1-S3, we estimate the number of proton-induced defects from its data. The highest number of detected dipoles in the whole quadrant read through amplifier 3 was 15,481, obtained from images at 160K. Considering that only traps under pixel phases 1 and 3 were probed, the trap density is estimated to be 0.134 traps/pixel after an irradiation of 1.2×10^{10} protons/cm² with

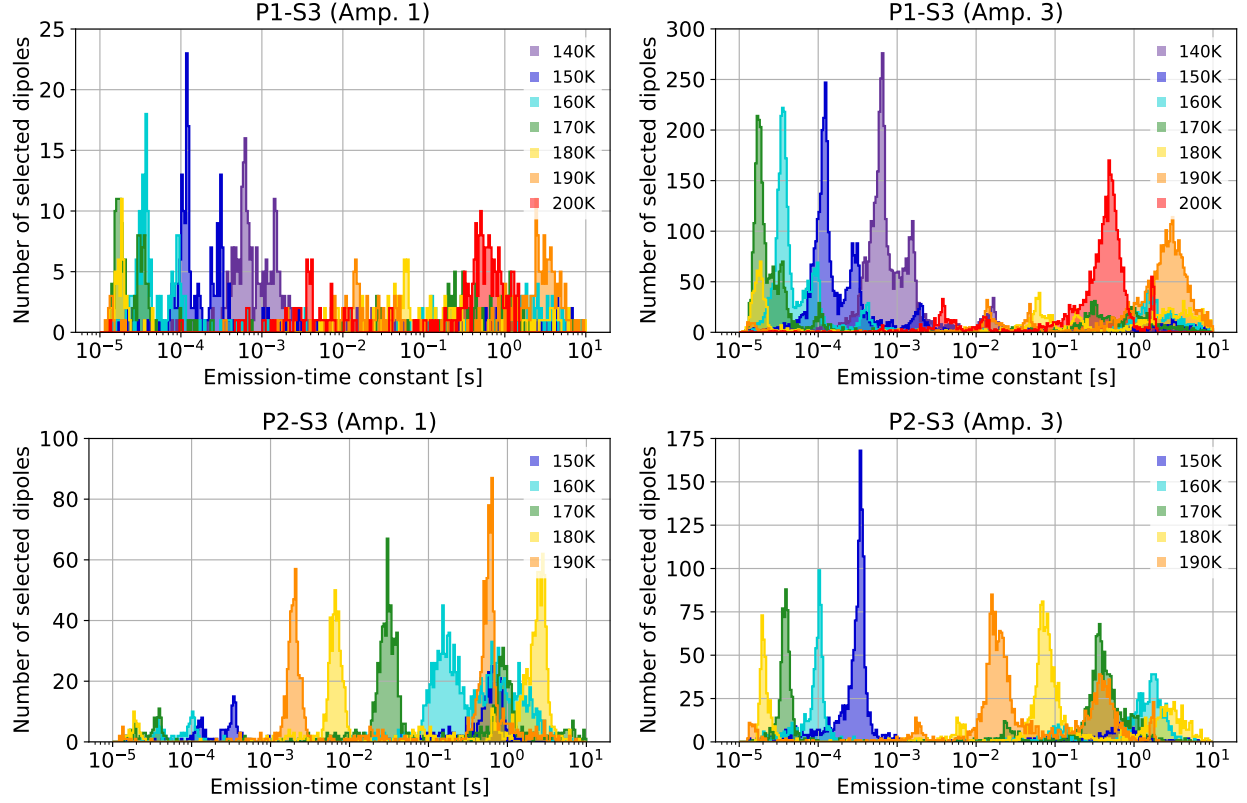


Figure 5: Histograms of the emission-time constants for the detected dipoles that passed the selection cuts in a $240 \text{ pix} \times 240 \text{ pix}$ region next to the readout amplifier at different temperatures. Dipoles were extracted from pocket-pumped images read out through amplifiers 1 (left) and 3 (right) in sensors P1-S3 (top) and P2-S3 (bottom).

217-MeV protons. It should be noted that the pocket pumping technique probes defects under a pixel within an approximate volume of $(10 \text{ } \mu\text{m})^3$ in the buried-channel.

As seen in the histograms in Fig. 5, trap emission-time constants depend on temperature. For p-channel CCDs, according to the Shockley-Read-Hall model for carrier generation and recombination [26], this dependence is given by

$$\tau_e = \frac{1}{\sigma v_{th} N_v} e^{\frac{E_t}{k_B T}} \quad \text{with} \quad v_{th} = \sqrt{\frac{3k_B T}{m_{\text{cond}}^h}} \quad \text{and} \quad N_v = 2 \left[2\pi m_{\text{dens}}^h \frac{k_B T}{h^2} \right]^{3/2}. \quad (2)$$

Here, k_B is the Boltzmann constant, T is temperature [K], E_t is the trap energy level [eV], σ is the trap cross section [cm^2], v_{th} is the charge-carrier's thermal velocity [cm/s], and N_v is the effective density of states in the valence band [cm^{-3}]. The dependence on T of v_{th} and N_v is also shown in Eq. 2, where m_{cond}^h is the hole effective mass for conductivity calculations, m_{dens}^h is the hole effective mass for density of states calculations, and h is the Planck constant. Between 100K and 200K, $m_{\text{cond}}^h \simeq 0.41m_e$ and $m_{\text{dens}}^h \simeq 0.94m_e$, with m_e the free electron rest mass [27].

For each selected trap in the histograms in Fig. 5, we plot τ_e as a function of T and fit it with the function in Eq. 2. From each of those fits, we extract the energy E_t and cross section σ associated to each trap. We select fits with a coefficient of determination greater than 0.7 and a relative error on E_t below 50%. The 2D histograms of the trap energies and cross sections from the selected fits are shown in Fig. 6. The local maxima within the histograms are associated with different trap species. From these maxima, we extract the characteristic parameters of the trap species and compare them with values reported in the literature.

This information is summarized in Tables 2 and 3.

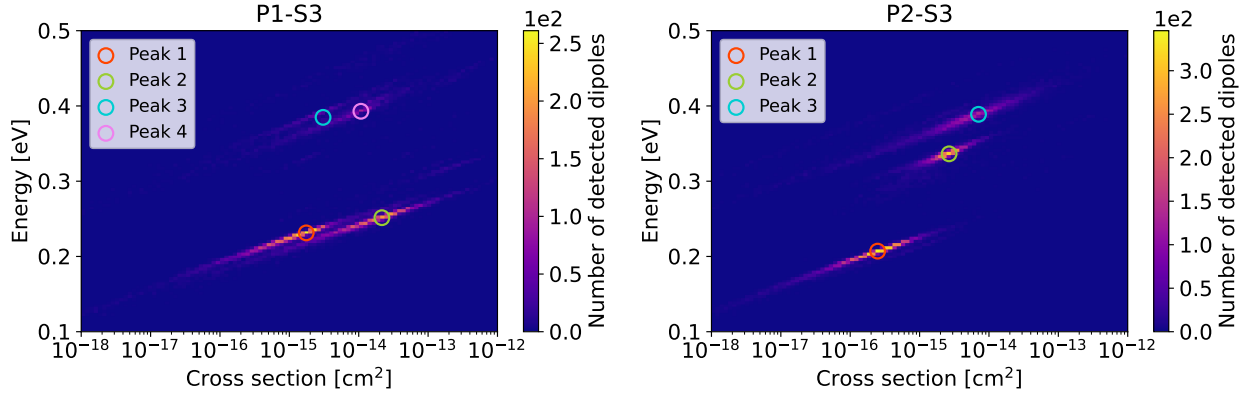


Figure 6: 2D histograms of the characteristic trap parameters extracted from the selected fits to τ_e as a function of T for each selected dipole in sensor P1-S3 (left) and P2-S3 (right). Local maxima associated with different trap species are marked as peaks.

P1-S3				
Peak No.	1	2	3	4
Energy [eV] ($E_t - E_v$)	0.231	0.252	0.389	0.393
Cross section [cm ²]	1.8×10^{-15}	2.2×10^{-14}	2.7×10^{-15}	1.1×10^{-14}
Trap species identification	V ₂	V _n O _m (?)	C _i O _i	C _i O _i (?)

Table 2: Characteristic trap parameters associated with each trap species found in sensor P1-S3. Species marked with (?) indicate uncertainty in their identification.

P2-S3			
Peak No.	1	2	3
Energy [eV] ($E_t - E_v$)	0.207	0.336	0.389
Cross section [cm ²]	2.5×10^{-16}	2.7×10^{-15}	7.1×10^{-15}
Trap species identification	V ₂	Traps from fabrication	C _i O _i

Table 3: Characteristic trap parameters associated with each trap species found in sensor P2-S3.

As discussed in the literature [11, 28, 29, 30], the divacancy is the dominant radiation-generated trap in p-channel CCDs with a donor level reported between $E_v + 0.18$ and 0.23 eV and a cross section ranging from 10^{-16} and 10^{-15} cm². From our results, we associate this defect with the population of traps related to peak 1 in both sensors, for which we report energies of $E_v + 0.21$ and 0.23 eV and cross sections of 2.5×10^{-16} and 1.8×10^{-15} cm². Also, we find that this trap species has the largest population.

The population of traps related to peak 2 in sensor P1-S3 could be associated with divacancy-oxygen complexes (V_nO_m). Interstitial oxygen, typically electrically inactive in silicon, is known to effectively trap divacancies, being the divacancy-oxygen interaction the primary mechanism for V₂ elimination after annealing at temperatures above 200°C [31, 32]. The V₂O hole trap has been reported to have an energy between $E_v + 0.23$ and 0.24 eV and a cross section on the order of 10^{-14} cm² [29, 31, 32, 33]. Although our sensors were stored and operated at temperatures between room temperature and ~ 140 K, conditions under which the formation of these defects from annealing is not expected, our measurements yield similar energy ($E_v + 0.25$ eV) and cross section (2.2×10^{-14} cm²) to those reported for V₂O.

We identify the traps associated with peak 3 in both sensors as belonging to the same species, with an energy of $E_v + 0.39$ eV and cross sections of 2.7×10^{-15} cm² and 7.1×10^{-15} cm². We associate this species to the

C_iO_i defect, which has been identified in previous work as a radiation-induced defect in p-type silicon [28, 29], reporting an energy between $E_v + 0.36$ and 0.39 eV and a cross section ranging from 10^{-15} and 10^{-14} cm^2 . Traps associated with peak 4 in sensor P1-S3 might also belong to the same species, as our results yield similar energy ($E_v + 0.39$ eV) and cross section (1.1×10^{-14} cm^2).

Finally, we identify the traps associated with peak 2 in sensor P2-S3 as traps from fabrication, with an energy of $E_v + 0.34$ eV and a cross section of 2.7×10^{-15} cm^2 . These traps were associated with possible metal impurities in previous work [25], reporting an energy of $E_v + 0.34$ eV and a cross section of 3×10^{-15} cm^2 for sensors from the same fabrication batch as sensor P2-S3.

The slight differences in the trap species energies found in this work compared to reported values in the literature can be attributed to minor variations in the defect structures. The trap species cross sections exhibit higher uncertainty than the energies, which is expected due to their strong dependence on local variables within the lattice, such as the electric field.

As discussed in Ref. [25], charge depositions from trap emission occur as deferred charge within an image when $t_{\text{pix}} < \tau_e < t_{\text{img}}$, where t_{img} is the image readout time and t_{pix} is the readout time between two consecutive pixels. Given the dependence of τ_e on T (Eq. 2), trapped charge is expected to be emitted after more pixels at lower temperatures for a given t_{pix} . As also noted in Ref. [25], to minimize the distance from the source at which trapped charge is emitted, τ_e can be decreased by increasing T and/or t_{pix} can be increased by lengthening the CCD clocking times or, in skipper-CCDs, by increasing N_{smp} . However, these approaches can lead to increased background from other temperature- and/or exposure-dependent sources, which may be undesirable for certain applications. Fig. 7 shows τ_e as a function of T for each of the trap species identified in each sensor, using the parameters summarized in Tables 2 and 3 as input. From these plots, we infer that the radiation-induced defect with the greatest impact on charge trapping and detrapping within an image, assuming typical CCD readout times and operating temperatures, is the C_iO_i . Conversely, although the V_2 defect has the largest population, its τ_e at typical CCD operating temperatures is small enough that it does not produce significant effects from charge trapping and emission processes within an image.

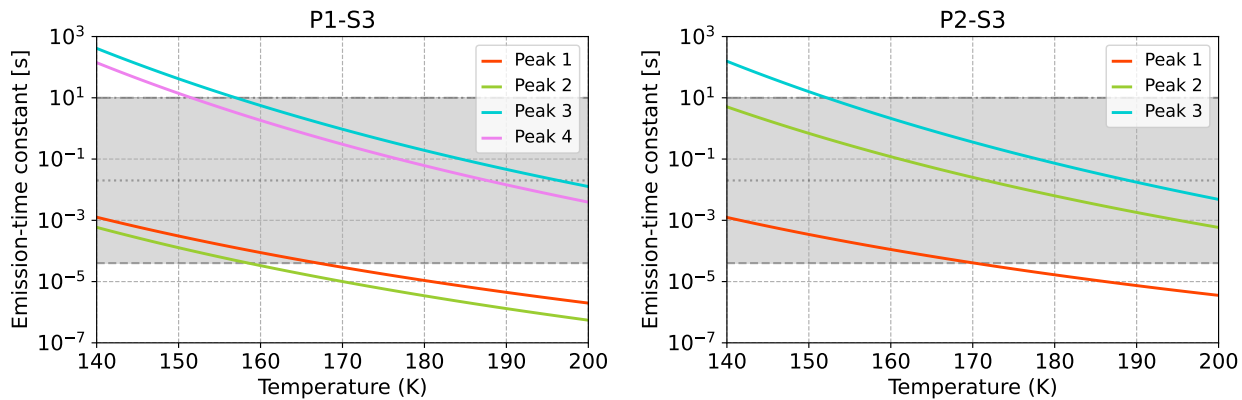


Figure 7: Emission-time constant as a function of T for each of the trap species identified in sensor P1-S3 (left) and P2-S3 (right), using the parameters summarized in Tables 2 and 3 as input. The gray horizontal lines indicate the time between two consecutive horizontal pixels (dashed), two consecutive vertical pixels (dotted), and the first and last pixels read in an image (dash-dotted), assuming a pixel readout time of $40 \mu\text{s}$ and an image size of $500 \text{ pix} \times 500 \text{ pix}$. Species with emission-time constants within the gray area will emit trapped charge within the image. With larger N_{smp} , the gray area shifts linearly toward larger τ_e .

3.3 Ionization damage

Output transistor curves

As discussed in the introduction, radiation-induced ionization damage can significantly impact CCD devices by changing the operating parameters of their intrinsic transistors, such as the threshold voltages. To evaluate ionization damage after irradiation, we measure the characteristic curves of the output transistors (I_{ds} as a function of $V_{gs} \equiv V_g - V_s$ and $V_{ds} = V_d - V_s$) in both sensors. Typically, the best operating voltages for the transistors to work as amplifiers are also determined from these curves.

A simplified diagram of the output stage of the skipper-CCDs tested in this work is shown in Fig. 8. To measure the characteristic curves of the output transistor (M1), we set the reset transistor (MR) to work in conduction mode so that $V_{ref} \equiv V_g$ in M1. We use an external power supply for V_{ref} to not be limited by the allowed voltage range from the LTA board. For each pair of $V_{dd} \equiv V_d$ and V_{ref} , we measure $V_{video} \equiv V_s$. The drain-source current of M1 is computed as $I_{ds} = -V_s/RL$, where RL is a load resistance of 20 k Ω .

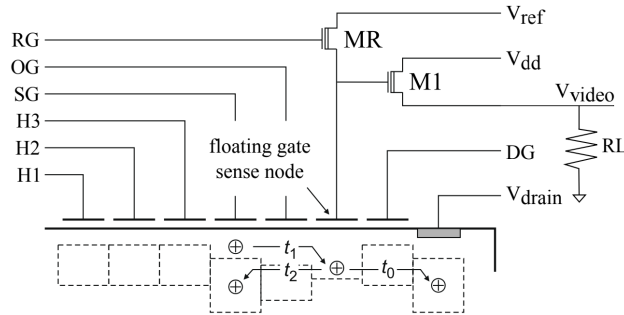


Figure 8: Taken from Ref. [34]. Simplified diagram of the skipper-CCDs output stage.

We measure the characteristic curves of all four output transistors in each sensor. During these measurements, the sensors were at 150K and typical operating biases were applied; in particular, the applied substrate voltage was 70V. Fig. 9 shows the I_{ds} vs. V_{gs} curves for different V_{ds} values (left) and the I_{ds} vs. V_{ds} curves for different V_{gs} values (right) for amplifier 1 in sensor P1-S3, as an example. This amplifier was not within the beam area during irradiation.

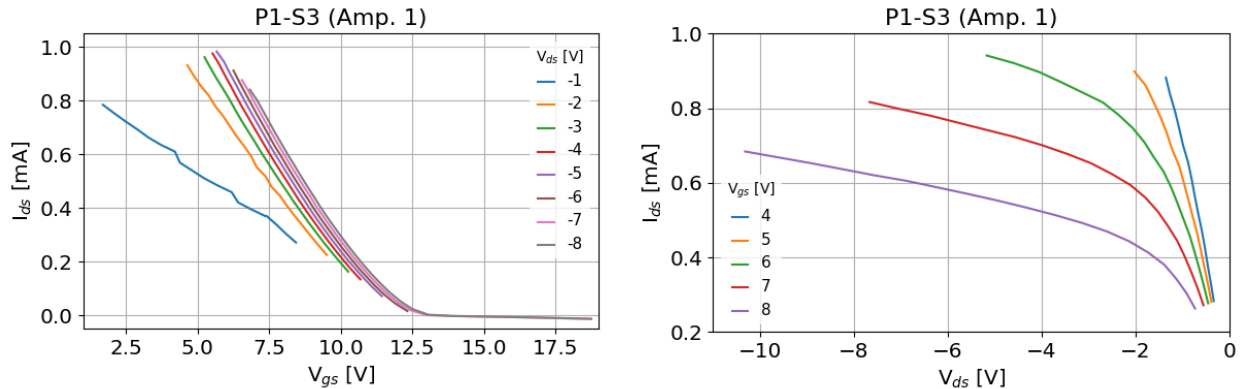


Figure 9: Characteristic curves of the amplifier 1 in sensor P1-S3. Left: I_{ds} as a function of V_{gs} for different V_{ds} . Right: I_{ds} as a function of V_{ds} for different V_{gs} .

The threshold voltage of the output transistor, V_t , can be extracted from the I_{ds} vs. V_{gs} curves, as it is

defined as the V_{gs} value for which $I_{ds} = 0$. The I_{ds} vs. V_{gs} curves for $V_{ds} = -7V$ for all amplifiers in each sensor are shown in Fig. 10. We find V_t to be consistent across amplifiers within the same sensor, regardless of whether they were within the beam area during irradiation, with $V_t = (12.8 \pm 0.3)V$ for amplifiers in sensor P1-S3 and $V_t = (11 \pm 0.2)V$ for amplifiers in sensor P2-S3. This consistency can be explained by the nature of voltage shifts, which are associated with trapped charge within the oxide layer. Such trapped charge results from unrecombined holes, and depends on the energy and type of incident radiation, the electron and hole mobilities (which in turn depend on temperature), and the electric field across the oxide. Additionally, trapped charge tends to neutralize at room temperature [35, 36]. Since the sensors were irradiated unbiased and at room temperature, conditions under which the formation of oxide-trapped charge is unlikely, no significant voltage shifts were observed. The difference in the V_t values between sensors is attributed to differences in the design of the output transistors.

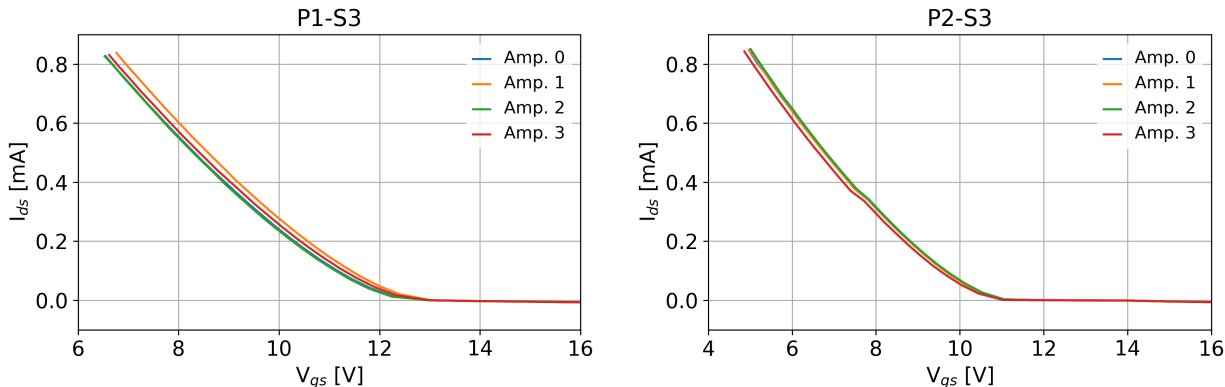


Figure 10: Curves I_{ds} as a function of V_{gs} for $V_{ds} = -7V$ of all the amplifiers in sensor P1-S3 (left) and P2-S3 (right). No radiation-induced voltage shifts were observed.

4 Conclusions

This work presents the detailed results of the characterization of proton-induced damage on thick, p-channel skipper-CCDs, an important step toward expanding the use of this technology in high-radiation environments. The sensors tested in this work were irradiated unbiased and at room temperature with 217-MeV protons, with fluences on the order of 10^{10} protons/cm², corresponding to displacement damage doses above 10^7 MeV/g.

Despite exposure to high proton fluences, both sensors preserved their ability to perform multiple non-destructive charge measurements, demonstrating single-electron/single-photon sensitivity [17]. This unique capability of skipper-CCDs, combined with their inherent spatial resolution, enables the precise identification of the effects of radiation-induced defects within an image, which appear as individual pixels with few-electron depositions, features that standard CCDs can only detect as increased charge-transfer inefficiency or higher dark counts.

Using the pocket-pumping technique, we quantified and identified the trap species associated with defects created after proton irradiation. The overall estimated trap density is 0.134 traps/pixel for a displacement damage dose of 2.3×10^7 MeV/g. Among the identified trap species, the divacancy, V_2 , has the largest population in both sensors, with emission-time constants τ_e below 1 ms for temperatures above 140K. However, its small τ_e compared to typical readout times minimizes its effects from charge trapping and emission processes within an image. In contrast, the C_iO_i defect, also found as trap species in both sensors, exhibited emission-time constants above 4 ms for temperatures below 200K, making it the proton-induced defect with the most significant impact on charge integrity within an image. The trap density associated to

this defect should depend strongly on the C and O concentrations within the silicon. Additionally, a third proton-induced trap species, potentially associated with divacancy-oxygen complexes from V₂ annealing, was identified in sensor P1-S3. However, this species has emission-time constants at operating temperatures similar to those of the divacancy, resulting in small effects from charge trapping and detrapping. The characteristic parameters associated with each trap species in the irradiated sensors are summarized in Tables 2 and 3.

Ionization damage was evaluated through measurements of the output transistor characteristic curves. No significant threshold voltage shifts were found for the output transistors of either sensor. This result is consistent with the conditions under which the sensors were irradiated, i.e. room temperature and unbiased, where oxide-trapped charge formation is unlikely.

The results from this work demonstrate the resilience of the skipper-CCDs output stage to proton irradiation and can be used as a guide to optimize their operating conditions mitigating the effects of radiation-induced damage in future applications, such as the proposed DarkNESS mission [37].

5 Acknowledgements

This work was done using the resources of the Fermi National Accelerator Laboratory (Fermilab), a U.S. Department of Energy, Office of Science, Office of High Energy Physics HEP User Facility. Fermilab is managed by Fermi Forward Discovery Group, LLC, acting under Contract No. 89243024CSC000002. This work was partially supported by NASA APRA award No. 80NSSC22K1411.

References

- [1] L. Barak, I. M. Bloch, M. Cababie, G. Cancelo, L. Chaplinsky, F. Chierchie, M. Crisler, A. Drlica-Wagner, R. Essig, J. Estrada, E. Etzion, G. F. Moroni, D. Gift, S. Munagavalasa, A. Orly, D. Rodrigues, A. Singal, M. S. Haro, L. Stefanazzi, J. Tiffenberg, S. Uemura, T. Volansky, and T.-T. Yu, “SENSEI: Direct-Detection Results on sub-GeV Dark Matter from a New Skipper-CCD,” *Phys. Rev. Lett.*, vol. 125, p. 171802, Oct 2020.
- [2] P. Adari, I. M. Bloch, A. M. Botti, M. Cababie, G. Cancelo, B. A. Cervantes-Vergara, M. Crisler, M. Daal, A. Desai, A. Drlica-Wagner, R. Essig, J. Estrada, E. Etzion, G. F. Moroni, S. E. Holland, J. Kehat, Y. Korn, I. Lawson, S. Luoma, A. Orly, S. E. Perez, D. Rodrigues, N. A. Saffold, S. Scorza, A. Singal, M. Sofo-Haro, L. Stefanazzi, K. Stifter, J. Tiffenberg, S. Uemura, E. M. Villalpando, T. Volansky, Y. Wu, T.-T. Yu, T. Emken, and H. Xu, “First Direct-Detection Results on Sub-GeV Dark Matter Using the SENSEI Detector at SNOLAB,” *Phys. Rev. Lett.*, vol. 134, p. 011804, Jan 2025.
- [3] I. Arnquist, N. Avalos, D. Baxter, X. Bertou, N. Castelló-Mor, A. Chavarria, J. Cuevas-Zepeda, J. C. Gutiérrez, J. Duarte-Campderros, A. Dastgheibi-Fard, O. Deligny, C. De Dominicis, E. Estrada, N. Gadola, R. Gañor, T. Hossbach, L. Iddir, L. Khalil, B. Kilminster, A. Lantero-Barreda, I. Lawson, S. Lee, A. Letessier-Selvon, P. Loaiza, A. Lopez-Virto, A. Matalon, S. Munagavalasa, K. McGuire, P. Mitra, D. Norcini, G. Papadopoulos, S. Paul, A. Piers, P. Privitera, K. Ramanathan, P. Robmann, M. Settimo, R. Smida, R. Thomas, M. Traina, I. Vila, R. Vilar, G. Warot, R. Yajur, and J.-P. Zopounidis, “First Constraints from DAMIC-M on Sub-GeV Dark-Matter Particles Interacting with Electrons,” *Phys. Rev. Lett.*, vol. 130, no. 17, p. 171003, 2023.
- [4] E. Marrufo Villalpando, A. Drlica-Wagner, B. Roach, M. Bonati, A. Bakshi, J. Campa, G. Cancelo, B. Cancino, C. R. Chavez, F. Chierchie, J. Estrada, G. Fernandez Moroni, L. Fraga, M. E. Gaido, S. E. Holland, R. Hur, M. Jonas, P. Moore, E. Paolini, A. A. Plazas Malagón, L. Stefanazzi, J. Tiffenberg, K. Treptou, S. Uemura, and N. Wilcer, “Astronomical spectroscopy with Skipper CCDs: first results from a Skipper CCD focal plane prototype at SIFS,” in *X-Ray, Optical, and Infrared Detectors for*

- Astronomy XI* (A. D. Holland and K. Minoglou, eds.), vol. 13103, p. 131030F, International Society for Optics and Photonics, SPIE, 2024.
- [5] M. Moll, *Radiation damage in silicon particle detectors: Microscopic defects and macroscopic properties*. PhD thesis, Hamburg U., Germany, 1999.
- [6] F. Hartmann, *Radiation Damage in Silicon Detector Devices*, pp. 177–214. Cham: Springer Nature Switzerland, 2024.
- [7] J. Janesick, T. Elliott, and F. Pool, “Radiation damage in scientific charge-coupled devices,” *IEEE Transactions on Nuclear Science*, vol. 36, no. 1, pp. 572–578, 1989.
- [8] T. Roy, S. Watts, and D. Wright, “Radiation damage effects on imaging charge coupled devices,” *Nuclear Instruments and Methods in Physics Research Section A: Accelerators, Spectrometers, Detectors and Associated Equipment*, vol. 275, no. 3, pp. 545–557, 1989.
- [9] G. Hopkinson, C. Dale, and P. Marshall, “Proton effects in charge-coupled devices,” *IEEE Transactions on Nuclear Science*, vol. 43, no. 2, pp. 614–627, 1996.
- [10] K. D. Stefanov, *Radiation Damage Effects in CCD Sensors for Tracking Applications in High Energy Physics*. PhD thesis, Saga U., Japan, 2001.
- [11] J. Spratt, B. Passenheim, and R. Leadon, “The effects of nuclear radiation on P-channel CCD imagers,” in *IEEE Radiation Effects Data Workshop NSREC Snowmass*, pp. 116–121, 1997.
- [12] G. Hopkinson, “Proton damage effects on p-channel CCDs,” *IEEE Transactions on Nuclear Science*, vol. 46, no. 6, pp. 1790–1796, 1999.
- [13] C. Bebek, D. Groom, S. Holland, A. Karcher, W. Kolbe, J. Lee, M. Levi, N. Palaio, B. Turko, M. Uslenghi, M. Wagner, and G. Wang, “Proton radiation damage in p-channel CCDs fabricated on high-resistivity silicon,” in *2001 IEEE Nuclear Science Symposium Conference Record (Cat. No.01CH37310)*, vol. 1, pp. 72–75, 2001.
- [14] J. Spratt, C. Conger, R. Bredthauer, W. Byers, R. Groulx, R. Leadon, and H. Clark, “Proton damage effects in high performance P-channel CCDs,” *IEEE Transactions on Nuclear Science*, vol. 52, no. 6, pp. 2695–2702, 2005.
- [15] J. R. Janesick, G. B. Soli, T. S. Elliott, and S. A. Collins, “Effects of proton damage on charge-coupled devices,” in *Charge-Coupled Devices and Solid State Optical Sensors II* (M. M. Blouke, ed.), vol. 1447, pp. 87 – 108, International Society for Optics and Photonics, SPIE, 1991.
- [16] B. A. Cervantes-Vergara, S. Perez, J. Estrada, A. Botti, C. R. Chavez, F. Chierchie, N. Saffold, A. Aguilar-Arevalo, F. Alcalde-Bessia, N. Avalos, O. Baez, D. Baxter, X. Bertou, C. Bonifazi, G. Canceledo, N. Castelló-Mor, A. E. Chavarria, J. M. D. Egea, J. C. D’Olivo, C. Dreyer, A. Drlica-Wagner, R. Essig, E. Estrada, E. Etzion, P. Grylls, G. Fernandez-Moroni, M. Fernández-Serra, S. Ferreyra, S. Holland, A. L. Barreda, A. Lathrop, I. Lawson, B. Loer, S. Luoma, E. M. Villalpando, M. M. Montero, K. McGuire, J. Molina, S. Munagavalasa, D. Norcini, A. Piers, P. Privitera, D. Rodrigues, R. Saldanha, A. Singal, R. Smida, M. Sofo-Haro, D. Stalder, L. Stefanazzi, J. Tiffenberg, M. Traina, S. Uemura, P. Ventura, R. V. Cortabitarte, and R. Yajur, “Skipper-CCD sensors for the Oscura experiment: requirements and preliminary tests,” *JINST*, vol. 18, p. P08016, aug 2023.
- [17] B. Roach, B. A. Cervantes-Vergara, S. Perez, A. Drlica-Wagner, J. Estrada, and A. Bakshi, “Effects of proton irradiation on the performance of skipper CCDs,” in *X-Ray, Optical, and Infrared Detectors for Astronomy XI* (A. D. Holland and K. Minoglou, eds.), vol. 13103, p. 131030G, International Society for Optics and Photonics, SPIE, 2024.
- [18] K. Dawson, C. Bebek, J. Emes, S. Holland, S. Jelinsky, A. Karcher, W. Kolbe, N. Palaio, N. Roe, J. Saha, K. Takasaki, and G. Wang, “Radiation Tolerance of Fully-Depleted P-Channel CCDs Designed for the SNAP Satellite,” *IEEE Transactions on Nuclear Science*, vol. 55, no. 3, pp. 1725–1735, 2008.

- [19] M. Boschini, P. Rancoita, and M. Tacconi, “SR-NIEL-7 Calculator: Screened Relativistic (SR) Treatment for NIEL Dose, Nuclear and Electronic Stopping Power Calculator (version 10.16),” 2014. Accessed on 02/13/2025.
- [20] G. Cancelo, C. Chavez, F. Chierchie, J. Estrada, G. F. Moroni, E. Paolini, M. S. Haro, A. Soto, L. Stefanazzi, J. Tiffenberg, *et al.*, “Low threshold acquisition controller for skipper charge-coupled devices,” *Journal of Astronomical Telescopes, Instruments, and Systems*, vol. 7, no. 1, pp. 015001–015001, 2021.
- [21] J. Janesick, *Scientific Charge-Coupled Devices*, vol. 83 of *Press Monograph*. SPIE, Jan. 2001.
- [22] M. M. Blouke, F. H. Yang, D. L. Heidtmann, and J. R. Janesick, “Traps and Deferred Charge in CCDs,” in *Instrumentation for Ground-Based Optical Astronomy* (L. B. Robinson, ed.), pp. 462–485, Springer, 1988.
- [23] D. J. Hall, N. J. Murray, A. D. Holland, J. Gow, A. Clarke, and D. Burt, “Determination of In Situ Trap Properties in CCDs Using a “Single-Trap Pumping” Technique,” *IEEE Transactions on Nuclear Science*, vol. 61, no. 4, pp. 1826–1833, 2014.
- [24] P. Bilgi, *Optimization of CCD charge transfer for ground and space-based astronomy*. PhD thesis, California Institute of Technology, Apr. 2019.
- [25] S. E. Perez Garcia, B. A. Cervantes Vergara, J. Cruz Estrada, S. Holland, D. P. Rodrigues Ferreira Maltez, and J. Tiffenberg, “Studying single-electron traps in newly fabricated Skipper-CCDs for the Oscura experiment using the pocket-pumping technique,” *Journal of Applied Physics*, vol. 136, p. 204502, 11 2024.
- [26] W. Shockley and W. T. Read, “Statistics of the Recombinations of Holes and Electrons,” *Phys. Rev.*, vol. 87, pp. 835–842, Sep 1952.
- [27] M. A. Green, “Intrinsic concentration, effective densities of states, and effective mass in silicon,” *Journal of Applied Physics*, vol. 67, no. 6, pp. 2944–2954, 1990.
- [28] C. Bebek, D. E. Groom, S. E. Holland, A. Karcher, W. F. Kolbe, J. S. Lee, M. E. Levi, N. P. Palaio, B. T. Turko, M. C. Uslenghi, M. T. Wagner, and G. Wang, “Proton radiation damage in high-resistivity n-type silicon CCDs,” in *Sensors and Camera Systems for Scientific, Industrial, and Digital Photography Applications III* (N. Sampat, J. Canosa, M. M. Blouke, J. Canosa, and N. Sampat, eds.), vol. 4669, pp. 161 – 171, International Society for Optics and Photonics, SPIE, 2002.
- [29] N. J. Mostek, C. J. Bebek, A. Karcher, W. F. Kolbe, N. A. Roe, and J. Thacker, “Charge trap identification for proton-irradiated p+ channel CCDs,” in *High Energy, Optical, and Infrared Detectors for Astronomy IV* (A. D. Holland and D. A. Dorn, eds.), vol. 7742, p. 774216, International Society for Optics and Photonics, SPIE, 2010.
- [30] D. Hall, D. Wood, N. Murray, J. Gow, A. Chronos, and A. Holland, “In situ trap properties in CCDs: the donor level of the silicon divacancy,” *Journal of Instrumentation*, vol. 12, p. P01025, jan 2017.
- [31] M. Trauwaert, J. Vanhellemont, H. E. Maes, A. Van Bavel, G. Langouche, and P. Clauws, “Low-temperature anneal of the divacancy in p-type silicon: A transformation from V2 to VxOy complexes?,” *Applied Physics Letters*, vol. 66, pp. 3056–3057, 05 1995.
- [32] M. Mikelsen, E. V. Monakhov, G. Alfieri, B. S. Avset, and B. G. Svensson, “Kinetics of divacancy annealing and divacancy-oxygen formation in oxygen-enriched high-purity silicon,” *Phys. Rev. B*, vol. 72, p. 195207, Nov 2005.
- [33] V. P. Markevich, A. R. Peaker, B. Hamilton, S. B. Lastovskii, and L. I. Murin, “Donor levels of the divacancy-oxygen defect in silicon,” *Journal of Applied Physics*, vol. 115, p. 012004, 01 2014.

- [34] J. Tiffenberg, M. Sofo-Haro, A. Drlica-Wagner, R. Essig, Y. Guardincerri, S. Holland, T. Volansky, and T.-T. Yu, “Single-Electron and Single-Photon Sensitivity with a Silicon Skipper CCD,” *Phys. Rev. Lett.*, vol. 119, p. 131802, Sept. 2017.
- [35] T. Oldham and F. McLean, “Total ionizing dose effects in MOS oxides and devices,” *IEEE Transactions on Nuclear Science*, vol. 50, no. 3, pp. 483–499, 2003.
- [36] J. R. Schwank, M. R. Shaneyfelt, D. M. Fleetwood, J. A. Felix, P. E. Dodd, P. Paillet, and V. Ferlet-Cavrois, “Radiation Effects in MOS Oxides,” *IEEE Transactions on Nuclear Science*, vol. 55, no. 4, pp. 1833–1853, 2008.
- [37] P. Alpine, S. Bhatia, F. Chierchie, A. Drlica-Wagner, R. Essig, J. Estrada, E. Etzion, R. Harnik, M. Lembeck, N. Saffold, *et al.*, “DarkNESS: developing a skipper-CCD instrument to search for Dark Matter from Low Earth Orbit,” tech. rep., Fermi National Accelerator Laboratory (FNAL), Batavia, IL (United States), 12 2024.